

Room Temperature Valley Polarization and Coherence in Transition Metal Dichalcogenide-Graphene van der Waals Heterostructures

Etienne Lorchat,^{1,*} Stefano Azzini,^{2,*} Thibault Chervy,^{2,*} Takashi Tanigushi,³ Kenji Watanabe,³ Thomas W. Ebbesen,² Cyriaque Genet,² and Stéphane Berciaud^{1,†}

¹ *Université de Strasbourg, CNRS, IPCMS, UMR 7504, F-67000 Strasbourg, France*

² *ISIS & icFRC, Université de Strasbourg and CNRS, UMR 7006, F-67000 Strasbourg, France*

³ *National Institute for Materials Science, Tsukuba, Ibaraki 305-0044, Japan*

Van der Waals heterostructures made of graphene and transition metal dichalcogenides (TMD) are an emerging platform for opto-electronic, -spintronic and -valleytronic devices that could benefit from (i) strong light-matter interactions and spin-valley locking in TMDs and (ii) exceptional electron and spin transport in graphene. The operation of such devices requires significant valley polarization and valley coherence, ideally up to room temperature. Here, using a comprehensive Mueller polarimetry analysis, we report *artifact-free* room temperature degrees of valley polarization up to 40 % and, remarkably, of valley coherence up to 20 % in monolayer tungsten disulfide (WS₂)/graphene heterostructures. Valley contrasts have been particularly elusive in molybdenum diselenide (MoSe₂), even at cryogenic temperatures. Upon interfacing monolayer MoSe₂ with graphene, the room temperature degrees of valley polarization and coherence are as high as 14 % and 20 %, respectively. Our results are discussed in light of recent reports of highly efficient inter-layer coupling and exciton transfer in TMD/graphene heterostructures and hold promise for room temperature chiral light-matter interactions and coherent opto-valleytronic devices.

Introduction – Semiconducting transition metal dichalcogenides (TMD, with formula MX₂, where M=Mo,W and X=S, Se, Te) are layered materials endowed with exceptional physical properties, which are promising for innovative two-dimensional opto-electronic and -valleytronic devices [1, 2]. In particular, monolayer TMD (1L-TMD) exhibit direct optical bandgaps and exciton binding energies around 20 times larger than the room temperature thermal energy [3]. Due to the combination of strong spin-orbit coupling and inversion symmetry breaking, 1L-TMD inherit spin-valley locked properties and chiral optical selection rules [4]. As a result, valley-polarized excitons [5–8] and their coherent superpositions [9] can be formed using circularly and lineary polarized light, respectively, and further manipulated using external fields [10–13].

Unfortunately, in pristine 1L-TMD, valley depolarization and valley decoherence occur on picosecond [14–17] and sub-picosecond [10–13] timescales, respectively. As a result, robust valley contrasting properties, have chiefly been demonstrated at cryogenic temperatures [2, 5–9, 14, 15], where the exciton lifetime is on the order of a few ps only [18], and where phonon induced intervalley scattering and pure dephasing are minimally efficient. A major challenge is therefore to preserve valley-contrasting properties up to room temperature (RT), where the *effective* exciton lifetime typically exceeds 100 ps in bare 1L-TMD [3, 18].

Room temperature valley polarization has been observed in bare 1L-MoS₂ [8] or WS₂ [19, 20], at the cost of a defect-induced reduction of the excitonic lifetime,

or, recently, in more complex assemblies, by strongly coupling 1L-WS₂ or 1L-MoS₂ excitons to an optical mode [21–24]. In this case, a cavity protection effect has been invoked to account for RT valley polarization. Noteworthy, valley coherence is directly sensitive to extrinsic and intrinsic pure dephasing mechanisms and hence much more fragile than valley polarization [13]. The largest degrees of valley coherence reported to date reach up to 55% at 4 K [25]. However, RT valley coherence has so far eluded experimental observation until our recent report of a steady state degree of valley coherence of 5 % to 8 % in WS₂ coupled to a plasmonic array [21]. Overall, obtaining robust RT valley contrasts in high-quality 1L-TMD is challenging but is, at the same time, a key prerequisite in view of emerging opto-spintronic and -valleytronic devices [26, 27]. Such devices typically interface (i) 1L-TMD as a chiral optical material and/or as an injector of spin/valley polarized electrons with (ii) graphene (Gr), as a high mobility channel for efficient spin-polarized electron transport [28–30]. In view of their obvious relevance for opto-valleytronics, valley polarization [31] and, crucially, valley coherence in 1L-TMD/Gr heterostructures deserve dedicated investigations.

In this letter, we investigate the valley contrasting properties of van der Waals heterostructures made of 1L-TMD and graphene. In these systems, highly efficient interlayer coupling leads to drastically shortened ($\lesssim 1$ ps) 1L-TMD exciton lifetime [32, 33] at RT. Valley-polarized excitons can thus quickly recombine radiatively or be directly transferred to graphene before undergoing intervalley scattering and dephasing processes. Using a comprehensive polarimetry analysis based on the Mueller formalism, we uncover RT degrees of valley polarization up to 40 % and, remarkably, RT degrees of valley coherence up to 20 % in high quality 1L-WS₂/Gr heterostructures. Valley contrasts have been particularly elusive in

* These authors contributed equally to this study

† stephane.berciaud@ipcms.unistra.fr

MoSe₂, even at cryogenic temperatures [34]. Upon interfacing 1L-MoSe₂ with graphene, we observe sizeable RT valley polarization of up to 14 % and valley coherence as high as 20 %. Robust RT valley coherence illustrates the high quality and homogeneity of our samples and opens many perspectives for coherent opto-valleytronic devices that take full benefit from the strong light-matter interactions and spin-valley locked properties of TMDs in combination with exceptional electron and spin transport in graphene.

Results – 1L-TMD/Gr heterostructures were fabricated from bulk WS₂, MoSe₂ and graphite crystals using a hot pick-up and transfer method introduced by Zomer *et al.* [35]. In order to get rid of environmental and substrate-induced perturbations, our 1L-TMD/Gr samples were encapsulated using thin layers of hexagonal boron nitride (BN) [25, 36]. The BN/WS₂/Gr/BN and The BN/MoSe₂/Gr/BN stacks were deposited onto transparent glass substrates so that polarization-resolved photoluminescence (PL) measurements could be performed in a transmission configuration. All measurements described below were performed in ambient air under sufficiently weak incoming photon flux (or pulse fluence) such that non-linear effects such as exciton-exciton annihilation [37] could be neglected.

Fig.1 shows (a) the structure and (b) an optical micrograph and a wide-field PL image (obtained using a UV lamp) of the WS₂-based sample. Differential reflectance (DR) spectra (recorded using a white light bulb), PL spectra, as well as PL decays are reported in Fig.1(c) and (d), respectively. The PL feature arises chiefly from band-edge (A) exciton recombination with a faint redshifted shoulder from charged excitons (trions) (see Fig. 2e,i). Due to enhanced dielectric screening from graphene, the PL from BN-capped WS₂/Gr (A exciton at 1.98 eV) is slightly redshifted as compared to BN-capped WS₂ (A exciton at 2.00 eV) [33, 38]. As previously reported, non-radiative exciton transfer from WS₂ to graphene leads to massive PL quenching (here, by a factor of ~ 250) and reduced exciton lifetime [32, 33], well below the temporal resolution of our setup (~ 50 ps). From the ≈ 120 ps RT exciton lifetime in BN-capped WS₂ we may estimate a RT exciton lifetime as short as ~ 500 fs in BN-capped WS₂/Gr. Similar measurements in BN-capped MoSe₂/Gr are reported in the Supporting Information, Fig. S9.

To date, valley polarization in TMDs has been assessed through measurements of the degree of circular polarization $\rho^\pm = \frac{I_{\sigma_\pm}^\pm - I_{\sigma_\mp}^\pm}{I_{\sigma_+}^\pm + I_{\sigma_-}^\pm}$, where $I_{\sigma_\pm}^{pm}$, $I_{\sigma_\mp}^{pm}$ denote the polarization-resolved σ_\pm components of the total PL intensity, following optical excitation with circularly polarized light (σ_\pm). Similarly, the degree of valley coherence has been considered equal to the degree of linear polarization $\gamma = \frac{I_{\parallel} - I_{\perp}}{I_{\parallel} + I_{\perp}}$, measured under linearly polarized excitation with an arbitrary orientation with respect to the TMD crystal lattice and where I_{\parallel} (resp. I_{\perp}) denote the PL intensity for parallel (resp. perpendicular) lin-

ear polarizations of the incoming and emitted photons. As explained in the Supporting Information (Sec. S2), this correspondence is only valid in the absence of any contribution from (i) circular or linear dichroism and (ii) polarization-dependent PL quantum yield. Owing to their highly symmetric hexagonal crystal structure (D_{3h} point group), 1L-TMDs feature isotropic absorption and emission following optical excitation polarized in the layer plane [3, 4]. However, polarization artifacts may arise when TMDs are hybridized to related two-dimensional materials, such as graphene.

In order to provide an *artifact-free* measurement of the valley contrasts, we make use of home-built polarimetry setup that allows us to measure the 4×4 Mueller matrix \mathcal{M} associated with the spatially and spectrally resolved PL response of our samples. The Mueller matrix connects arbitrary incoming polarization states (defined by the Stokes vector of the incoming laser beam) to the outgoing Stokes vector associated with the light emitted by the sample (see Refs. 39, 40 and Supporting Information, Sec. S2 and Fig. S1 for details). In the present study, the most relevant elements of the Mueller matrix are its diagonal terms m_{ii} , with $i = 0..3$. By definition, m_{00} corresponds to the PL intensity and is normalized to unity at all measured wavelengths. Hence, the PL spectra shown in Fig. 2a,e and Fig. 3a,e in arbitrary units correspond to m_{00} recorded under unpolarized excitation, without any polarization analysis and prior normalization. With this definition of m_{00} , the degrees of valley polarization and valley coherence are directly given by m_{33} and m_{11} (or m_{22}), respectively. Circular and linear dichroism are corresponding to m_{03} and m_{01} , m_{02} , respectively, whereas polarization-dependent PL quantum yields are accounted for by m_{i0} , $i = 1..3$. In the Mueller formalism, $i = 1$ (resp. $i = 2$) refer to vertical/horizontal (resp. $\pm 45^\circ$) linear polarizations relative to an arbitrary reference angle. Based on symmetry properties, \mathcal{M} is expected to be diagonal in bare 1L-TMDs, with $m_{11} = m_{22}$.

Figure 2 displays the spatially and spectrally resolved diagonal elements of the Mueller matrix of the sample shown in Fig.1. The maps in Fig. 2a-d correspond to spectrally integrated PL intensity (Fig. 2a), valley coherence ($m_{11,22}$, Fig. 2b,c) and valley polarization m_{33} upon laser excitation at 1.96 eV. A clear anti-correlation between the total PL intensity and the valley contrasts appears, with near zero valley contrasts in BN-capped WS₂ (bright regions in Fig. 1b and 2a) and large degrees of valley polarization and coherence in BN-capped WS₂/Gr. To quantitatively assess the valley contrasts, we resort to spectrally resolved measurements at two different laser excitation energies, very close to (1.96 eV, i.e., 633 nm, see Fig. 2e-h) or slightly above (2.07 eV, i.e., 600 nm, see Fig. 2i-l) the optical bandgap of BN-capped WS₂/Gr. In stark contrast with the total absence of valley contrasts in our BN-capped WS₂ sample ($m_{ii,i=1..3} \approx 0$), BN-capped WS₂/Gr exhibits large valley polarization ($m_{33} \approx 40\%$) and coherence ($m_{11} \approx m_{22} \approx 20\%$) over the entire span of the PL spectrum. In Fig. 2f-h, these contrasts give

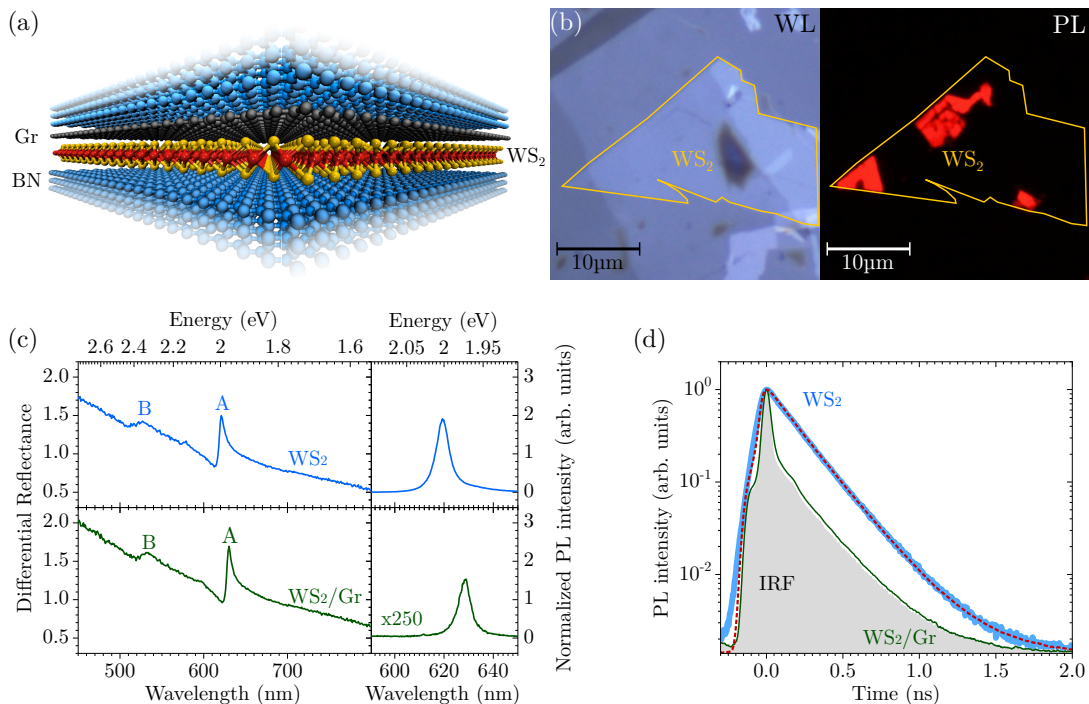


FIG. 1. (a) Schematic of a BN-capped 1L-WS₂/Gr heterostructure. (b) White light (WL) and photoluminescence (PL) image of a BN-capped 1L-WS₂/Gr sample. Dark yellow lines highlight the WS₂ monolayer. (c) Differential reflectance (DR) and PL spectra of BN-capped 1L-WS₂ (blue) and BN-capped 1L-WS₂/Gr (green). The PL spectra were recorded in the linear regime, under *cw* laser illumination at 532 nm (2.33 eV). (d) PL decay of BN-capped 1L-WS₂ (blue solid line) and BN-capped 1L-WS₂/Gr (green solid line) recorded under pulsed excitation at 480 nm (2.58 eV). The instrument response function (IRF) is represented by the grey area. The red dashed line is a mono-exponential fit to the BN-capped WS₂ PL decay yielding an exciton lifetime of 120 ps.

rise to a baseline on which five sharp peaks with larger contrasts emerge. These peaks correspond to a faint laser residue, and to polarization sensitive Stokes and anti-Stokes Raman scattering features from (i) the out-of-plane A'_1 phonon (near 1.907 eV on the Stokes side) and (ii) the resonant 2LA(M) mode (near 1.915 eV on the Stokes side) [41]. Note that the in-plane E' feature expected to overlap with the 2LA(M) feature but has vanishingly small intensity under laser excitation at 1.96 eV. The proposed assignments are unambiguously confirmed by high-resolution polarized Raman measurements (see Supporting Information, Fig. S8).

Very similar results are observed (Fig. 2i-l) when exciting the sample at 2.07 eV, except for the fact that no spurious contributions from Raman features are observed. Similar valley contrasts were observed in another BN-capped WS₂/Gr sample and in SiO₂-supported WS₂/Gr samples either exposed to ambient air (not shown) or covered by a LiF epilayer (see Supporting Information, Fig. S5).

Motivated by the observation of large RT valley contrasts in WS₂/Gr, we now consider the Mueller matrix of MoSe₂/Gr. Indeed, no significant valley polarization has been reported so far in bare MoSe₂, even at low tempera-

ture. The microscopic mechanism responsible for accelerated valley depolarization and decoherence in MoSe₂ remains a topic of ongoing research [3, 34]. Figure 3 shows the PL spectra and $m_{ii,i=1..3}$ in BN-capped MoSe₂/Gr compared to a reference in a BN-capped MoSe₂ sample, wherein a short excitonic lifetime (and thus potentially measurable valley contrasts) was observed (see Supporting Information, Fig. S9). The A exciton in BN-capped MoSe₂/Gr (resp. BN-capped MoSe₂) is found at 1.568 eV (resp. 1.573 eV) and the higher order B exciton lies near 1.77 eV. Under quasi resonant excitation at 1.59 eV (i.e., 780 nm, see Fig. 3a-d), we measure a degree of valley polarization $m_{33} \approx 14\%$ near the A exciton peak energy in BN-capped MoSe₂/Gr. Remarkably, the RT degree of valley coherence $m_{11,22} \approx 20\%$ in BN-capped MoSe₂/Gr exceeds m_{33} . Conversely, $m_{11,22} \approx 5\%$ and $m_{33} \approx 2\%$ in BN-capped MoSe₂. Under excitation at 1.77 eV (i.e., 700 nm, see Fig. 3a-d), slightly above the spin-split B exciton, we observe vanishingly small valley contrasts associated with the A exciton. However, “hot” PL from the B exciton exhibits a large degree of valley polarization and coherence, both up to 40 % (resp. 35 %) in BN-capped MoSe₂/Gr (resp. BN-capped MoSe₂). Interestingly, similar valley contrasts are also observed under

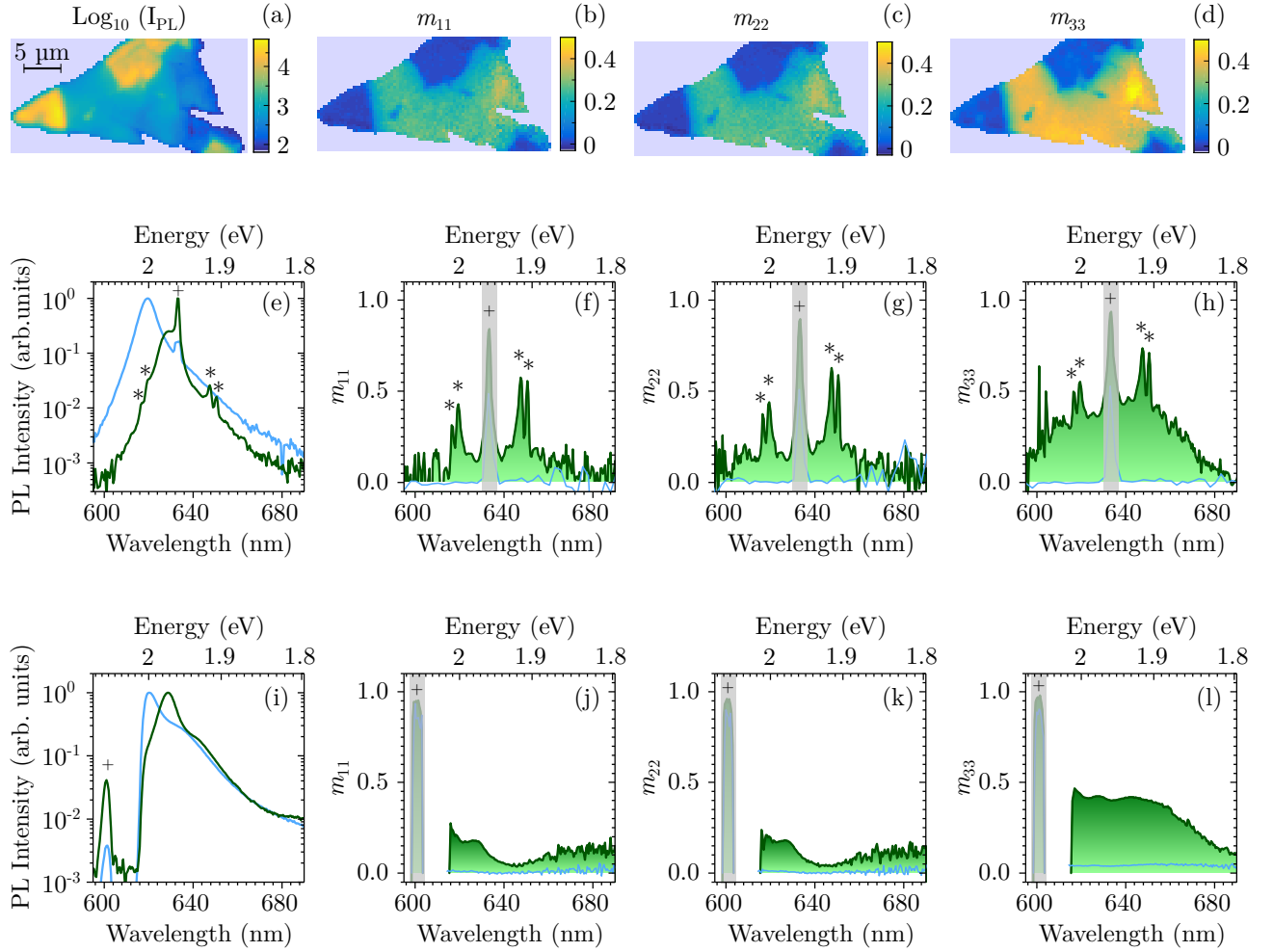


FIG. 2. Spatially resolved PL (a) intensity and (b)-(d) diagonal terms of the Mueller matrix (m_{ii} , $i = 1, 2, 3$) of the BN-capped WS_2/Gr sample shown in Fig.1 under optical excitation at 1.96 eV. PL spectra (e) and spectrally-resolved (f)-(h) diagonal terms of the Mueller matrix, under optical excitation at 1.96 eV (e)-(h) and 2.07 eV (i)-(l). The green (blue) curves correspond to BN-capped WS_2/Gr (BN-capped WS_2). Ultra narrow notch filters (Optigrate), were used for measurements at 1.96 eV (see (e)-(h)) in order to record the full resonant PL spectrum. The + and * symbols in (e)-(h) highlight residual contributions from the laser beam and polarization contrasts from WS_2 Raman scattering features, respectively. Note that, in (j),(k) the slight increase of $m_{11,22}$ on the low-energy wing of the WS_2 PL spectrum arises from the faint polarized Raman background from graphene.

excitation at 1.50 eV (i.e., 825 nm), slightly below the MoSe_2 bandgap (see Supporting Information, Fig. S7).

Discussion – Our study demonstrates that robust RT valley polarization and coherence can now be generated optically in systems based on 1L-TMD, including in MoSe_2 , where such contrasts had not yet been reported so far. Importantly, using Mueller polarimetry in 1L-TMD/Gr heterostructures, we experimentally demonstrate that $m_{11} = m_{22}$ and that $m_{ij, j \neq i} \approx 0$ (see Supporting Information, Figs. S2-S4 and S6), such that circular dichroism and birefringence can be safely neglected in these systems.

At the microscopic level, RT valley contrasts in our TMD/Gr samples are a direct consequence of highly efficient non-radiative exciton transfer from 1L-TMD to

Gr [33]. Exciton transfer restricts the observation of radiative recombination of valley polarized excitons and of their coherent superpositions to short ($\lesssim 1$ ps) timescales that are comparable with typical valley polarization and decoherence times. In other words, as illustrated in Fig. 4, excitons that would undergo intervalley scattering and dephasing processes in bare 1L-TMD are efficiently filtered out by the near-field coupled graphene layer. Along this line, valley contrasts associated with B exciton emission in MoSe_2 and MoSe_2/Gr (see Fig. 3f-h) also stem from the sub-ps lifetime of these higher-order states.

Assuming full valley polarization under circularly polarized *cw* excitation, we can estimate a steady state de-

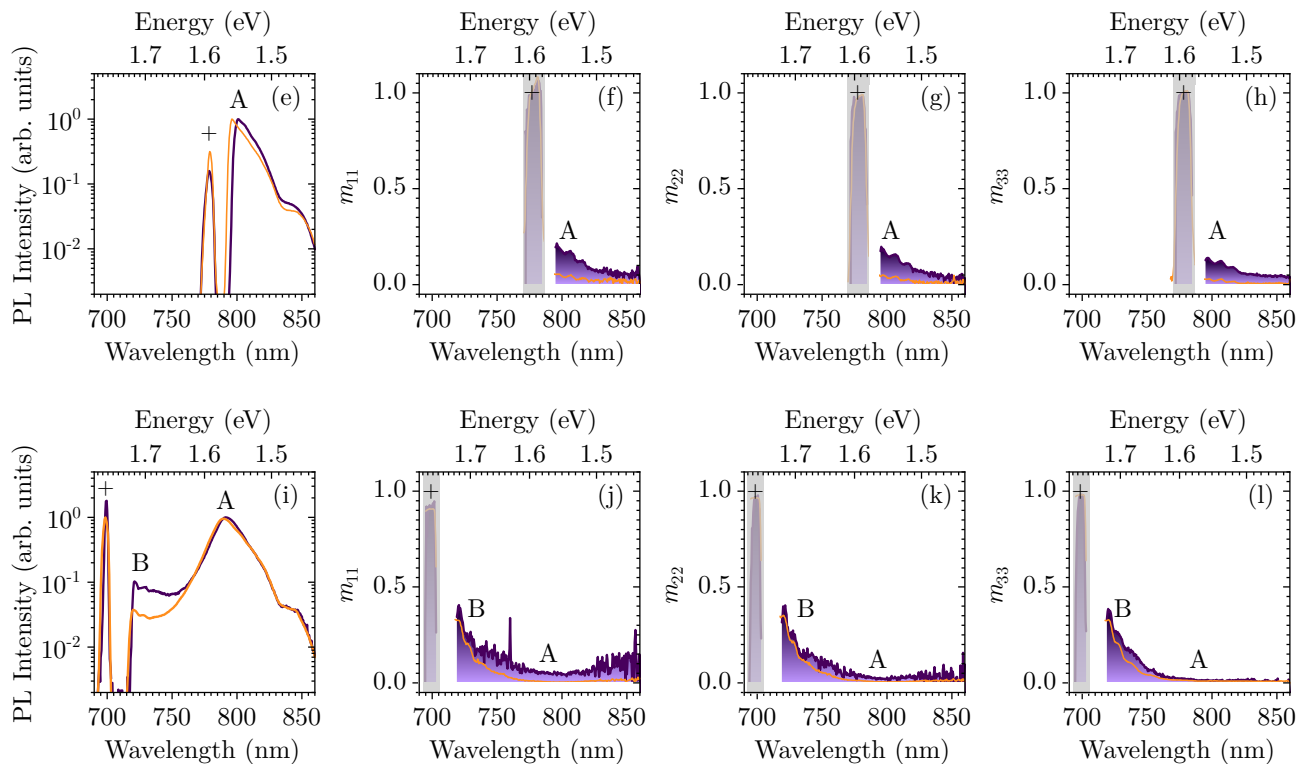


FIG. 3. PL spectra and spectrally resolved diagonal terms of the Mueller matrix (m_{ii} , $i = 1, 2, 3$) of a BN-capped MoSe₂/Gr sample under optical excitation at 780 nm (i.e., 1.59 eV) (a)-(d), and 700 nm (i.e., 1.77 eV) (e)-(h). The purple (resp. orange) curves correspond to BN-capped MoSe₂/Gr (resp. BN-capped MoSe₂). The + symbols highlight residual contributions from the laser beam. The locations of the A and B exciton features are indicated.

degree of valley polarization $m_{33} = \left(1 + 2\frac{\Gamma_{\text{KK}'}}{\Gamma_{\text{X}}}\right)^{-1}$, where Γ_{X} denotes the exciton decay rate and $\Gamma_{\text{KK}'}$ the intervalley spin scattering rate, respectively [5] (see also Fig 4). Assuming $\Gamma_{\text{X}}^{-1} \approx 500$ fs, and considering our measured values of m_{33} , we estimate $\Gamma_{\text{KK}' }^{-1} \approx 600$ fs in WS₂/Gr and $\Gamma_{\text{KK}' }^{-1} \approx 150$ fs in MoSe₂/Gr. The fact that the degree of valley coherence $m_{11,22}$ is approaching (in WS₂/Gr) or exceeding (in MoSe₂/Gr) m_{33} indicates that the dominant intervalley scattering mechanism that limits valley polarization is almost exclusively responsible for valley decoherence. Indeed, when pure dephasing is negligible, the valley-exciton decoherence time is twice the lifetime of the valley exciton polarization [42]. Such a near ideal case had so far only been reported in BN-capped MoS₂ at 4 K [25]. At present, intervalley exciton scattering mediated by the exchange interaction is thought to be the dominant valley depolarization and decoherence mechanism [3, 9, 13, 43]. Alternate mechanisms based on electron-phonon interactions have also been proposed [17]. Temperature dependent Mueller polarimetry in TMD/Gr samples should help unravel the relative contributions from both mechanisms.

We note that the valley contrasts reported above come at the cost of significant PL quenching and short exciton lifetimes. Nevertheless, the PL intensity in TMD/Gr has

recently been shown to scale linearly with the incident photon fluxes up to values in excess of 10^{24} cm⁻²s⁻¹ (i.e., typically a visible laser beam of 1 mW focused onto a diffraction limited spot [33]). In contrast, under these conditions, the PL efficiency of bare 1L-TMD is massively reduced due to exciton-exciton annihilation effects and lies close to that of 1L-TMD/Gr [33]. More broadly, 1L-TMD/Gr heterostructures feature major advantages as compared to related systems, in which RT valley contrasts have recently been unveiled. First, even in the absence of BN capping layers, 1L-TMD/Gr have been shown to be well-defined systems with smooth interfaces and highly reproducible photophysical properties [33]. RT valley contrasts can thus consistently be observed in minimally defective TMD/Gr samples. This result is in stark contrast with recent reports in bare 1L-TMD, in which RT valley polarization -and so far, not valley coherence- are observable only when structural defects or extrinsic environmental effects provide sufficiently fast non-radiative exciton decay pathways to bypass intervalley scattering [20]. Second, RT valley contrasts have also recently been reported in bare bilayer and few-layer TMD [43, 44]. In bilayer and even N-layer TMD, inversion symmetry *a priori* precludes the observation of valley contrasting properties and recent observation of circularly polarized emission [43] may either

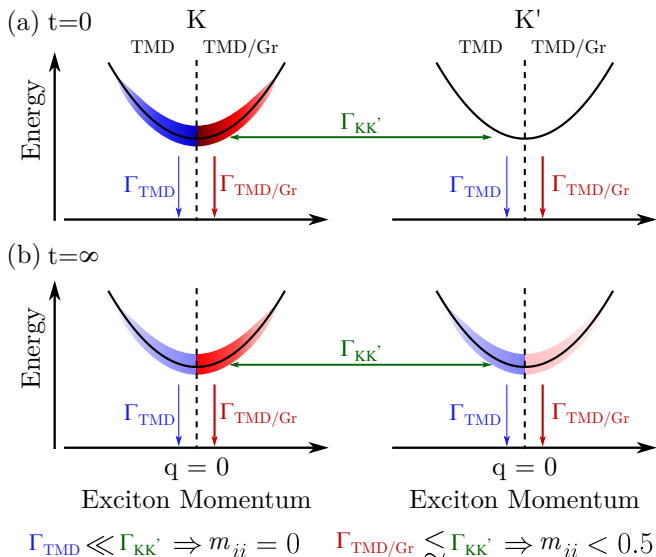


FIG. 4. Sketches, in the momentum-energy space, of valley-exciton dynamics in bare 1L-TMD compared to 1L-TMD/Gr. Γ_X , with $X = \text{TMD}, \text{TMD/Gr}$ denote the band-edge exciton decay rate of the bare 1L-TMD and of the 1L-TMD/Gr heterostructure, respectively. $\Gamma_{\text{KK}'}$ is the intervalley scattering rate. Exciton populations in each valley are illustrated with blue (TMD) and red (TMD/Gr) contours. Darker shades correspond to larger populations. The top panel (a) depicts full valley polarization following optical pumping using circularly polarized photons. The bottom panel (b) represents the populations of valley excitons in the steady state.

have an extrinsic origin or may be due to A exciton confinement in a 1L unit [4] or arise from spin polarization rather than from valley polarization [45]. Mueller polarimetry could help settle such debates and determine whether finite degrees of circular or linear polarization in such systems stem from valley polarization and coherence or from the off-diagonal terms of the Mueller matrix. In addition, although RT valley contrasts are symmetry-allowed and have been reported in odd N-layer WS_2 [44], these systems feature indirect optical bandgaps (alike bilayer TMD) and very small PL efficiencies as compared to 1L-TMD/Gr. Last but not least, owing to

the excellent electron and spin transport properties of Gr, 1L-TMD/Gr can easily be electrically connected and integrated in chiral light emitting systems [46] and opto-spintronic circuits [26, 27].

Conclusion – We have demonstrated that monolayer transition metal dichalcogenides (here, WS_2 and MoSe_2) directly stacked onto monolayer graphene provide highly stable room temperature chiral light emitters, in spite of inevitable photoluminescence quenching. Similar valley contrasting properties are expected in related systems such as MoS_2 , WSe_2 and possibly near-infrared emitters, such as MoTe_2 [47, 48], where, as in bare MoSe_2 , valley contrasts remain elusive [49]. Our complete analysis, based on the Mueller formalism provides *artifact-free* measurements of valley polarization and valley coherence. As such, it goes beyond state of the art polarimetry in transition metal dichalcogenides, which so far has relied on measurements of circular and linear polarization contrasts [3, 4, 9, 50]. We anticipate further implementations of Mueller polarimetry to investigate chiral light-matter interactions not only in transition metal dichalcogenides (in particular in bilayer or few-layer systems) but also in other emerging two-dimensional systems, such as two-dimensional ferromagnets [51] and van der Waals heterostructures based on the latter [52]. Besides direct implementations in novel opto-valleytronic devices, robust generation of room temperature valley-polarized excitons and, importantly, of valley coherence invite further investigations in nano-photonics, in particular in the chiral strong coupling regime [21].

Supporting Information – Additional details on methods. Mueller polarimetry. Full Mueller matrices measured on BN-capped WS_2/Gr and BN-capped MoSe_2/Gr . Helicity resolved PL spectra on $\text{WS}_2/\text{graphene}$. High resolution Raman measurements on WS_2/Gr . Optical characterization of BN-capped $\text{MoSe}_2/\text{graphene}$.

Acknowledgements – We thank the STNano clean room staff for technical assistance, J. Hone and D. Chenet for valuable advice on sample fabrication. This work was supported in part by the ANR Equipex “Union” (ANR-10-EQPX-52-01), ANR Grant (H2DH ANR-15-CE24-0016), the Labex NIE projects (ANR-11-LABX-0058-NIE) and USIAS within the Investissement d’Avenir program ANR-10-IDEX-0002-02. S.B. is a member of the Institut Universitaire de France (IUF).

- [1] Kin Fai Mak and Jie Shan, “Photonics and optoelectronics of 2D semiconductor transition metal dichalcogenides,” *Nat. Photonics* **10**, 216–226 (2016).
- [2] John R Schaibley, Hongyi Yu, Genevieve Clark, Pasqual Rivera, Jason S Ross, Kyle L Seyler, Wang Yao, and Xiaodong Xu, “Valleytronics in 2D materials,” *Nature Reviews Materials* **1**, 16055 (2016).
- [3] Gang Wang, Alexey Chernikov, Mikhail M. Glazov, Tony F. Heinz, Xavier Marie, Thierry Amand, and Bern-

- hard Urbaszek, “Colloquium: Excitons in atomically thin transition metal dichalcogenides,” *Rev. Mod. Phys.* **90**, 021001 (2018).
- [4] Xiaodong Xu, Wang Yao, Di Xiao, and Tony F. Heinz, “Spin and pseudospins in layered transition metal dichalcogenides,” *Nat. Phys.* **10**, 343–350 (2014).
- [5] Kin Fai Mak, Keliang He, Jie Shan, and Tony F Heinz, “Control of valley polarization in monolayer MoS_2 by optical helicity,” *Nat. Nanotechnol.* **7**, 494–498 (2012).

- [6] Hualing Zeng, Junfeng Dai, Wang Yao, Di Xiao, and Xiaodong Cui, “Valley polarization in MoS_2 monolayers by optical pumping,” *Nature nanotechnology* **7**, 490–493 (2012).
- [7] Ting Cao, Gang Wang, Wenpeng Han, Huiqi Ye, Chuanrui Zhu, Junren Shi, Qian Niu, Pingheng Tan, Enge Wang, Baoli Liu, and Ji Feng, “Valley-selective circular dichroism of monolayer molybdenum disulphide,” *Nature Communications* **3**, 887 (2012).
- [8] G. Sallen, L. Bouet, X. Marie, G. Wang, C. R. Zhu, W. P. Han, Y. Lu, P. H. Tan, T. Amand, B. L. Liu, and B. Urbaszek, “Robust optical emission polarization in MoS_2 monolayers through selective valley excitation,” *Phys. Rev. B* **86**, 081301 (2012).
- [9] Aaron M Jones, Hongyi Yu, Nirmal J Ghimire, Sanfeng Wu, Grant Aivazian, Jason S Ross, Bo Zhao, Jiaqiang Yan, David G Mandrus, Di Xiao, W Yao, and X Xu, “Optical generation of excitonic valley coherence in monolayer WSe_2 ,” *Nat. Nanotechnol.* **8**, 634–638 (2013).
- [10] Ziliang Ye, Dezheng Sun, and Tony F. Heinz, “Optical manipulation of valley pseudospin,” *Nature Physics* **13**, 26 (2016).
- [11] G. Wang, X. Marie, B. L. Liu, T. Amand, C. Robert, F. Cadiz, P. Renucci, and B. Urbaszek, “Control of exciton valley coherence in transition metal dichalcogenide monolayers,” *Phys. Rev. Lett.* **117**, 187401 (2016).
- [12] Robert Schmidt, Ashish Arora, Gerd Plechinger, Philipp Nagler, Andrés Granados del Águila, Mariana V. Ballotín, Peter C. M. Christianen, Steffen Michaelis de Vasconcellos, Christian Schüller, Tobias Korn, and Rudolf Bratschitsch, “Magnetic-field-induced rotation of polarized light emission from monolayer WS_2 ,” *Phys. Rev. Lett.* **117**, 077402 (2016).
- [13] Kai Hao, Galan Moody, Fengcheng Wu, Chandriker Kavir Dass, Lixiang Xu, Chang-Hsiao Chen, Liuyang Sun, Ming-Yang Li, Lain-Jong Li, Allan H. MacDonald, and Xiaoqin Li, “Direct measurement of exciton valley coherence in monolayer WSe_2 ,” *Nature Physics* **12**, 677 (2016).
- [14] D. Lagarde, L. Bouet, X. Marie, C. R. Zhu, B. L. Liu, T. Amand, P. H. Tan, and B. Urbaszek, “Carrier and polarization dynamics in monolayer MoS_2 ,” *Phys. Rev. Lett.* **112**, 047401 (2014).
- [15] G. Wang, L. Bouet, D. Lagarde, M. Vidal, A. Balocchi, T. Amand, X. Marie, and B. Urbaszek, “Valley dynamics probed through charged and neutral exciton emission in monolayer WSe_2 ,” *Phys. Rev. B* **90**, 075413 (2014).
- [16] C. R. Zhu, K. Zhang, M. Glazov, B. Urbaszek, T. Amand, Z. W. Ji, B. L. Liu, and X. Marie, “Exciton valley dynamics probed by kerr rotation in WS_2 monolayers,” *Phys. Rev. B* **90**, 161302 (2014).
- [17] Alejandro Molina-Sánchez, Davide Sangalli, Ludger Wirtz, and Andrea Marini, “Ab initio calculations of ultrashort carrier dynamics in two-dimensional materials: Valley depolarization in single-layer WSe_2 ,” *Nano Letters* **17**, 4549–4555 (2017).
- [18] C. Robert, D. Lagarde, F. Cadiz, G. Wang, B. Lassagne, T. Amand, A. Balocchi, P. Renucci, S. Tongay, B. Urbaszek, and X. Marie, “Exciton radiative lifetime in transition metal dichalcogenide monolayers,” *Phys. Rev. B* **93**, 205423 (2016).
- [19] Pramoda K. Nayak, Fan-Cheng Lin, Chao-Hui Yeh, Jer-Shing Huang, and Po-Wen Chiu, “Robust room temperature valley polarization in monolayer and bilayer WS_2 ,” *Nanoscale* **8**, 6035–6042 (2016).
- [20] Kathleen M. McCreary, Marc Currie, Aubrey T. Hanbicki, Hsun-Jen Chuang, and Berend T. Jonker, “Understanding variations in circularly polarized photoluminescence in monolayer transition metal dichalcogenides,” *ACS Nano* **11**, 7988–7994 (2017).
- [21] Thibault Chervy, Stefano Azzini, Etienne Lorchat, Shaojun Wang, Yuri Gorodetski, James A. Hutchison, Stéphane Berciaud, Thomas W. Ebbesen, and Cyriaque Genet, “Room temperature chiral coupling of valley excitons with spin-momentum locked surface plasmons,” *ACS Photonics* , doi:10.1021/acsp Photonics.7b01032 (2018).
- [22] Yen-Jung Chen, Jeffrey D. Cain, Teodor K. Stanev, Vinayak P. Dravid, and Nathaniel P. Stern, “Valley-polarized exciton-polaritons in a monolayer semiconductor,” *Nature Photonics* **11**, 431 (2017).
- [23] Zheng Sun, Jie Gu, Areg Ghazaryan, Zav Shotan, Christopher R. Consideine, Michael Dollar, Biswanath Chakraborty, Xiaozhe Liu, Pouyan Ghaemi, Stéphane Kéna-Cohen, and Vinod M. Menon, “Optical control of room-temperature valley polaritons,” *Nature Photonics* **11**, 491 (2017).
- [24] N. Lundt, S. Stoll, P. Nagler, A. Nalitov, S. Klemmt, S. Betzold, J. Goddard, E. Frieling, A. V. Kavokin, C. Schüller, T. Korn, S. Höfling, and C. Schneider, “Observation of macroscopic valley-polarized monolayer exciton-polaritons at room temperature,” *Phys. Rev. B* **96**, 241403 (2017).
- [25] F. Cadiz, E. Courtade, C. Robert, G. Wang, Y. Shen, H. Cai, T. Taniguchi, K. Watanabe, H. Carrere, D. Lagarde, M. Manca, T. Amand, P. Renucci, S. Tongay, X. Marie, and B. Urbaszek, “Excitonic linewidth approaching the homogeneous limit in MoS_2 -based van der Waals heterostructures,” *Phys. Rev. X* **7**, 021026 (2017).
- [26] Yunqiu Kelly Luo, Jinsong Xu, Tiancong Zhu, Guanzhong Wu, Elizabeth J. McCormick, Wenbo Zhan, Mahesh R. Neupane, and Roland K. Kawakami, “Opto-valleytronic spin injection in monolayer MoS_2 /few-layer graphene hybrid spin valves,” *Nano Letters* **17**, 3877–3883 (2017).
- [27] Ahmet Avsar, Dmitrii Unuchek, Jiawei Liu, Oriol Lopez Sanchez, Kenji Watanabe, Takashi Taniguchi, Barbaros Zylmaz, and Andras Kis, “Optospintronics in graphene via proximity coupling,” *ACS Nano* **11** (2017).
- [28] Wei Han, Roland K Kawakami, Martin Gmitra, and Jaroslav Fabian, “Graphene spintronics,” *Nature nanotechnology* **9**, 794 (2014).
- [29] Talieh S. Ghiasi, Josep Ingla-Ayns, Alexey A. Kaverzin, and Bart J. van Wees, “Large proximity-induced spin lifetime anisotropy in transition-metal dichalcogenide/graphene heterostructures,” *Nano Letters* **17**, 7528–7532 (2017).
- [30] L. Antonio Benítez, Juan F. Sierra, Williams Savero Torres, Alois Arrighi, Frédéric Bonell, Marius V. Costache, and Sergio O. Valenzuela, “Strongly anisotropic spin relaxation in graphene-transition metal dichalcogenide heterostructures at room temperature,” *Nature Physics* **14**, 303 (2017).
- [31] Luoju Du, Qian Zhang, Benchao Gong, Mengzhou Liao, Jianqi Zhu, Hua Yu, Rui He, Kai Liu, Rong Yang, Dongxia Shi, Lin Gu, Feng Yan, Guangyu Zhang, and

- Qingming Zhang, “Robust spin-valley polarization in commensurate MoS₂/graphene heterostructures,” *Phys. Rev. B* **97**, 115445 (2018).
- [32] Jiaqi He, Nardeep Kumar, Matthew Z Bellus, Hsin-Ying Chiu, Dawei He, Yongsheng Wang, and Hui Zhao, “Electron transfer and coupling in graphene–tungsten disulfide van der Waals heterostructures,” *Nat. Commun.* **5** (2014).
- [33] Guillaume Froehlicher, Etienne Lorchat, and Stéphane Berciaud, “Charge versus energy transfer in atomically thin graphene-transition metal dichalcogenide van der waals heterostructures,” *Phys. Rev. X* **8**, 011007 (2018).
- [34] G. Wang, E. Palleau, T. Amand, S. Tongay, X. Marie, and B. Urbaszek, “Polarization and time-resolved photoluminescence spectroscopy of excitons in MoSe₂ monolayers,” *Appl. Phys. Lett.* **106**, 112101 (2015).
- [35] P. J. Zomer, M. H. D. Guimarães, J. C. Brant, N. Tombros, and B. J. van Wees, “Fast pick up technique for high quality heterostructures of bilayer graphene and hexagonal boron nitride,” *Appl. Phys. Lett.* **105**, 013101 (2014).
- [36] Obafunso A Ajayi, Jenny V Ardelean, Gabriella D Shepard, Jue Wang, Abhinandan Antony, Takeshi Taniguchi, Kenji Watanabe, Tony F Heinz, Stefan Strauf, X-Y Zhu, and James C Hone, “Approaching the intrinsic photoluminescence linewidth in transition metal dichalcogenide monolayers,” *2D Materials* **4**, 031011 (2017).
- [37] Nardeep Kumar, Qiannan Cui, Frank Ceballos, Dawei He, Yongsheng Wang, and Hui Zhao, “Exciton-exciton annihilation in MoSe₂ monolayers,” *Phys. Rev. B* **89**, 125427 (2014).
- [38] Archana Raja, Andrey Chaves, Jaeun Yu, Ghidon Arefe, Heather M. Hill, Albert F. Rigosi, Timothy C. Berkelbach, Philipp Nagler, Christian Schiller, Tobias Korn, Colin Nuckolls, James Hone, Louis E. Brus, Tony F. Heinz, David R. Reichman, and Alexey Chernikov, “Coulomb engineering of the bandgap and excitons in two-dimensional materials,” *Nature Communications* **8**, 15251 (2017).
- [39] Christian Brosseau, *Fundamentals of polarized light* (Wiley-Interscience, 1998).
- [40] F Le Roy-Brehonnet and B Le Jeune, “Utilization of mueller matrix formalism to obtain optical targets depolarization and polarization properties,” *Progress in Quantum Electronics* **21**, 109–151 (1997).
- [41] Ayse Berkdemir, Humberto R. Gutierrez, Andrs R. Botello-Mndez, Néstor Perea-López, Ana Laura Elías, Chen-Ing Chia, Bei Wang, Vincent H. Crespi, Florentino Lopez-Uras, Jean-Christophe Charlier, Humberto Terrones, and Mauricio Terrones, “Identification of individual and few layers of WS₂ using raman spectroscopy,” *Scientific Reports* **3**, 1755 (2013).
- [42] M. Z. Maialle, E. A. de Andrada e Silva, and L. J. Sham, “Exciton spin dynamics in quantum wells,” *Phys. Rev. B* **47**, 15776–15788 (1993).
- [43] Bairen Zhu, Hualing Zeng, Junfeng Dai, Zhirui Gong, and Xiaodong Cui, “Anomalously robust valley polarization and valley coherence in bilayer WS₂,” *PNAS* **111**, 11606–11611 (2014).
- [44] R Suzuki, M Sakano, YJ Zhang, R Akashi, D Morikawa, A Harasawa, K Yaji, K Kuroda, K Miyamoto, T Okuda, K Ishizaka, R Arita, and Y Iwasa, “Valley-dependent spin polarization in bulk mos 2 with broken inversion symmetry,” *Nature nanotechnology* **9**, 611 (2014).
- [45] Qihang Liu, Xiuwen Zhang, and Alex Zunger, “Intrinsic Circular Polarization in Centrosymmetric Stacks of Transition-Metal Dichalcogenide Compounds,” *Phys. Rev. Lett.* **114**, 087402 (2015).
- [46] Y. J. Zhang, T. Oka, R. Suzuki, J. T. Ye, and Y. Iwasa, “Electrically Switchable Chiral Light-Emitting Transistor,” *Science* **344**, 725–728 (2014).
- [47] Claudia Ruppert, Ozgur Burak Aslan, and Tony F. Heinz, “Optical Properties and Band Gap of Single- and Few-Layer MoTe₂ Crystals,” *Nano Lett.* **14**, 6231–6236 (2014).
- [48] Guillaume Froehlicher, Etienne Lorchat, and Stéphane Berciaud, “Direct versus indirect band gap emission and exciton-exciton annihilation in atomically thin molybdenum ditelluride (MoTe₂),” *Phys. Rev. B* **94**, 085429 (2016).
- [49] C. Robert, R. Picard, D. Lagarde, G. Wang, J. P. Echeverry, F. Cadiz, P. Renucci, A. Högele, T. Amand, X. Marie, I. C. Gerber, and B. Urbaszek, “Excitonic properties of semiconducting monolayer and bilayer MoTe₂,” *Phys. Rev. B* **94**, 155425 (2016).
- [50] Andre Neumann, Jessica Lindlau, Léo Colombier, Manuel Nutz, Sina Najmaei, Jun Lou, Aditya D. Mohite, Hisato Yamaguchi, and Alexander Högele, “Opto-valleytronic imaging of atomically thin semiconductors,” *Nature Nanotechnology* **12**, 329–334.
- [51] Kyle L. Seyler, Ding Zhong, Dahlia R. Klein, Shiyuan Gao, Xiaou Zhang, Bevin Huang, Efrn Navarro-Moratalla, Li Yang, David H. Cobden, Michael A. McGuire, Wang Yao, Di Xiao, Pablo Jarillo-Herrero, and Xiaodong Xu, “Ligand-field helical luminescence in a 2D ferromagnetic insulator,” *Nature Physics* **14**, 277 (2018).
- [52] Ding Zhong, Kyle L. Seyler, Xiayu Linpeng, Ran Cheng, Nikhil Sivadas, Bevin Huang, Emma Schmidgall, Takashi Taniguchi, Kenji Watanabe, Michael A. McGuire, Wang Yao, Di Xiao, Kai-Mei C. Fu, and Xiaodong Xu, “Van der waals engineering of ferromagnetic semiconductor heterostructures for spin and valleytronics,” *Science Advances* **3**, e1603113 (2017).
- [53] Aaron M Jones, Hongyi Yu, John R Schaibley, Jiaqiang Yan, David G Mandrus, Takashi Taniguchi, Kenji Watanabe, Hanan Dery, Wang Yao, and Xiaodong Xu, “Excitonic luminescence upconversion in a two-dimensional semiconductor,” *Nat. Phys.* **12**, 323–327 (2016).
- [54] M Manca, MM Glazov, C Robert, F Cadiz, T Taniguchi, K Watanabe, E Courtade, T Amand, P Renucci, X Marie, G Wang, and B Urbaszek, “Enabling valley selective exciton scattering in monolayer wse 2 through upconversion,” *Nature communications* **8**, 14927 (2017).

Supporting Information

S1. METHODS SUMMARY

We fabricate our BN-capped TMD/Graphene samples by a hot pick-up method introduced by Zomer *et al.* [35]. First, we exfoliate bulk crystals on Silicon wafers coated with a 90 nm oxide epilayer. Then we identify flakes of interest, including TMD and Gr monolayers that we characterize by optical contrast and micro-PL and/or micro-Raman spectroscopy. Starting from the top capping BN layer, layers of choice (graphene, TMD and bottom BN) are sequentially picked up using a polycarbonate (PC) coated polydimethylsiloxane (PDMS) stamp. The stack is finally transferred onto a 170 μm thick glass coverslip held at a controlled temperature. Finally, PC residues are eliminated in chloroform.

Differential reflectance, PL (including PL decays) and Raman spectra were recorded using a home-built micro-optical spectroscopy setup, as in Ref. 33. DR measurements were performed using a white-light bulb. PL and Raman spectra were recorded using *cw* lasers either at 532 nm or 633 nm. Time-correlated PL measurements (Fig. 1 and S9) were performed using the filtered output of a supercontinuum light source at 480 nm (~ 50 ps pulse duration) and a single photon counting board. The supercontinuum source was also employed for all polarization-resolved measurements, except those performed at 633 nm, where a *cw* HeNe laser was used. All measurements described below were performed in ambient air under sufficiently weak incoming photon flux (or pulse fluence) such that non-linear effects such as exciton-exciton annihilation could be neglected.

The Mueller polarimetry setup is described in more details below.

S2. PL MUELLER POLARIMETRY

The optical setup shown in Fig.S1 is used to run Mueller polarimetry of the PL emission from our 1L-MX₂/Gr hetero-structures, namely measuring PL spectra for different combinations of excitation and detection polarizations. Such measurements allow us to retrieve the full Mueller matrix \mathcal{M} of the sample, a spectral characterization of how the polarization state of the emitted PL is related to the polarization state of the excitation beam, allowing us in particular to retrieve the valley polarization and coherence of the material.

S2.1. Mueller matrix and Stokes vector

The emission Mueller matrix \mathcal{M} of a given material system determines the polarization state of the PL emission given that a pump beam with a certain polarization state is providing the excitation. An incident excitation in a given polarization state is defined by a Stokes vector \mathbf{S}^{in} , on which the matrix \mathcal{M} acts to yield an output PL Stokes vector \mathbf{S}^{out} :

$$\mathbf{S}^{\text{out}} = \begin{pmatrix} I \\ I_V - I_H \\ I_{45} - I_{-45} \\ I_{\sigma^+} - I_{\sigma^-} \end{pmatrix}_{\text{out}} = \mathcal{M} \cdot \mathbf{S}^{\text{in}} = \mathcal{M} \begin{pmatrix} I_0 \\ I_V - I_H \\ I_{45} - I_{-45} \\ I_{\sigma^+} - I_{\sigma^-} \end{pmatrix}_{\text{in}}, \quad (\text{S1})$$

where $I_{(0)}$ is the emitted (incident) intensity, $I_V - I_H$ is the relative intensity in vertical and horizontal polarizations, $I_{45} - I_{-45}$ is the relative intensity in $+45^\circ$ and -45° polarizations and $I_{\sigma^+} - I_{\sigma^-}$ is the relative intensity in σ^+ and σ^- polarizations, and \mathcal{M} is a 4×4 matrix generally expressed in the form:

$$\mathcal{M} = \begin{pmatrix} m_{00} & m_{01} & m_{02} & m_{03} \\ m_{10} & m_{11} & m_{12} & m_{13} \\ m_{20} & m_{21} & m_{22} & m_{23} \\ m_{30} & m_{31} & m_{32} & m_{33} \end{pmatrix}. \quad (\text{S2})$$

S2.2. Experimental setup and methods

Spectrally resolved Mueller matrices of the PL emission from our samples are obtained by means of the optical setup sketched in Fig.S1, where the optical elements composing the Mueller polarimeter are highlighted. The polarimeter is formed by two stages (both comprising a linear polarizer and a quarter-wave plate), one for the preparation and another one for the analysis of the polarization state of light before and after the sample, respectively. The linear polarizer employed in the preparation stage represents the first polarization optics on the beam path, which is setting the linear state to vertical. On the other hand, in the analysis stage, the last element is a linear polarizer set to horizontal, ensuring a well-defined polarization state for the detection line. Two broadband quarter-wave plates mounted on rotating motors are used for both preparing and analyzing a given polarization state before and after the sample, respectively. We adopt a measurement protocol [40] for which each wave-plate is rotated across 8 different angular positions of the fast axis by a 22.5° angular step, resulting in a total number of 64 measurements for a full reconstruction of the Mueller matrix. For each measurement a spectrum is recorded corresponding to the S_0 coefficient of the output Stokes vector for a given combination (θ_1, θ_2) of prepared and analyzed polarization states :

$$\mathbf{S}^{\text{out}} = \mathcal{M}_{\text{H-LP}} \mathcal{M}_{\lambda/4}(\theta_2) \mathcal{M} \mathcal{M}_{\lambda/4}(\theta_1) \mathcal{M}_{\text{V-LP}} \mathbf{S}^{\text{in}}. \quad (\text{S3})$$

The Mueller matrices of the horizontal and vertical polarizers ($\mathcal{M}_{\text{H(V)-LP}}$) are taken as ideal polarizing elements (extinction ratio $> 10^5 : 1$), while the wave-plates are modelled by homogeneous elliptical birefringent (HEB) elements. The wavelength dependent ellipticity and retardance of these two HEB waveplates are obtained from transmission measurement under white light illumination and in the absence of the sample, by minimizing the deviations of the reconstructed Mueller matrix from an identity matrix. The algebraic problem is overdetermined, consisting of 64 equations for 16 unknowns, so that the Mueller matrix is reconstructed by a pseudo-inversion operation. The determined parameters of the wave-plates are subsequently inserted in the same HEB model which is used for getting the Mueller matrix of a PL emission experiment run on our 1L-MX₂/Gr hetero-structures. Note that this broadband calibration procedure of our Mueller polarimeter allows us to accurately account for any chromatic distortion of the polarization states of both the pump and the PL signal throughout the whole calibration range (550 – 850 nm).

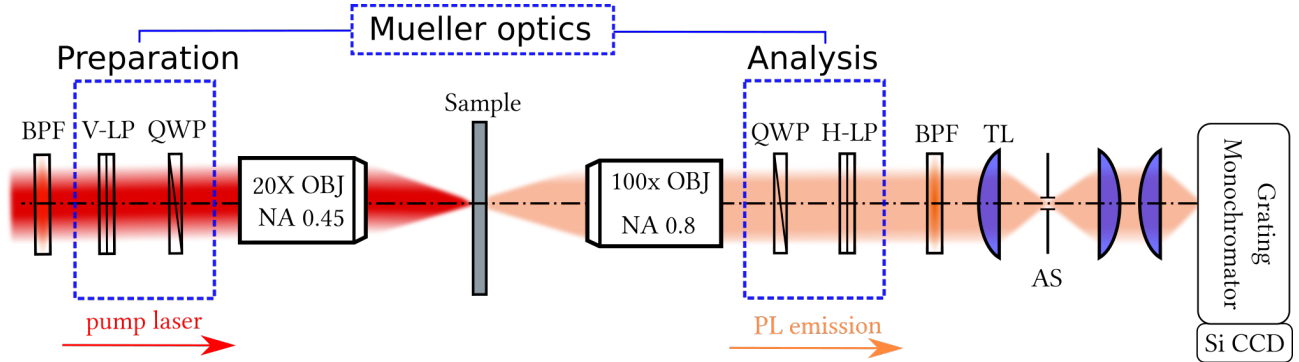


FIG. S1. PL Mueller polarimetry setup. BPF: band-pass filter, V-LP/H-LP: vertical/horizontal linear polarizers, QWP: quarter waveplate, TL: tube lens, NA: numerical aperture.

S2.3. Valley polarization and coherence from the Mueller matrix

The degrees of valley polarization and valley coherence are directly given by m_{33} and m_{11} (or m_{22}), respectively. These parameters correspond to the circular (m_{33}) and linear (m_{11} , m_{22}) polarization contrasts in the absence of any contribution from (i) circular (m_{03}) or linear (m_{01} , m_{02}) dichroism and (ii) polarization-dependent PL quantum yield (i.e., $m_{i0} = 0$).

In most reports on valley contrasting properties in TMDs, the valley polarization is assumed to be equal to the degree of circularly polarized PL emission under the same circularly polarized excitation, and it can be expressed using the following formula:

$$\rho^\pm = \frac{I_{\sigma^\pm}(\sigma^+) - I_{\sigma^\pm}(\sigma^-)}{I_{\sigma^\pm}(\sigma^+) + I_{\sigma^\pm}(\sigma^-)}, \quad (\text{S4})$$

where $I_j(l)$ is the measured PL spectrum for a $j = (\sigma^+, \sigma^-)$ polarized excitation and a $l = (\sigma^+, \sigma^-)$ polarized analysis. In a similar way, the valley coherence is usually taken equal to the degree of linearly polarized PL emission under the same linearly polarized excitation, and it can be expressed in two ways according to the chosen pair of linearly polarized states:

$$\gamma^{VH} = \frac{I_{V,H}(V) - I_{V,H}(H)}{I_{V,H}(V) + I_{V,H}(H)}, \quad (\text{S5})$$

$$\gamma^{+45^\circ - 45^\circ} = \frac{I_{+45^\circ - 45^\circ}(+45^\circ) - I_{+45^\circ - 45^\circ}(-45^\circ)}{I_{+45^\circ - 45^\circ}(+45^\circ) + I_{+45^\circ - 45^\circ}(-45^\circ)}, \quad (\text{S6})$$

where $I_j(l)$ is the measured PL spectrum for a $j = (V, H)$ or $j = (+45^\circ, -45^\circ)$ polarized excitation and a $l = (V, H)$ or $l = (+45^\circ, -45^\circ)$ polarized analysis. Eq. S5 is for vertical (V) and horizontal (H) states, while Eq. S6 stands for $+45^\circ$ and -45° linear polarizations.

Using the Mueller-Stokes formalism, these contrasts can be expressed in terms of the elements of the Mueller matrix, by taking as measured total intensities the first elements $S_0 = I$ of the outgoing Stokes vectors.

Considering that the incoming Stokes vectors for $V, H, \pm 45^\circ, \sigma^\pm$ polarizations write:

$$\mathbf{S}_{V,H}^{\text{in}} = \begin{pmatrix} 1 \\ \pm 1 \\ 0 \\ 0 \end{pmatrix}_{V,H}, \quad \mathbf{S}_{45^\circ, -45^\circ}^{\text{in}} = \begin{pmatrix} 1 \\ 0 \\ \pm 1 \\ 0 \end{pmatrix}_{45^\circ, -45^\circ}, \quad \mathbf{S}_{\sigma^+, \sigma^-}^{\text{in}} = \begin{pmatrix} 1 \\ 0 \\ 0 \\ \pm 1 \end{pmatrix}_{\sigma^+, \sigma^-}, \quad (\text{S7})$$

we may then, by fixing the polarization state of the input pump beam, and taking the normalized difference of the total intensities under crossed polarization analysis, we obtain the expressions for γ^{VH} , $\rho^{45^\circ, -45^\circ}$ and ρ^\pm as a function of the Mueller matrix elements:

$$\gamma^{VH} = \frac{m_{10} + m_{11}}{m_{00} + m_{01}}, \quad \gamma^{+45^\circ, -45^\circ} = \frac{m_{20} + m_{22}}{m_{00} + m_{02}}, \quad \rho^\pm = \frac{m_{30} \pm m_{33}}{m_{00} \pm m_{03}}. \quad (\text{S8})$$

These simple expressions reveal that if the amplitude of the off-diagonal elements of \mathcal{M} is either zero or negligible, the valley polarization and coherence are respectively given by the m_{33} and m_{11} (or alternatively m_{22}) elements of the Mueller matrix, normalized with respect to m_{00} . In main the manuscript, we have, at each wavelength, normalized m_{00} to unity, such that the *unpolarized* PL spectra shown in Fig. 2 and 3 correspond to the *un-normalized* m_{00} .

Owing to their highly symmetric crystal structure, 1L-TMDs feature isotropic absorption and emission following optical excitation polarized in the layer plane [3, 4]. As a result, all the off-diagonal elements of \mathcal{M} vanish and $m_{11} = m_{22}$. These symmetry arguments justify why, in 1L-TMDs, the degrees of valley polarization (m_{33}) and valley coherence (m_{11}, m_{22}) have thus far been approximated by the helicity parameter ρ^\pm and by the degree of linear polarization γ (for an arbitrary incoming linear polarization), respectively.

S3. SUPPLEMENTARY FIGURES

Full Mueller matrices recorded for BN-capped WS₂/Gr (see Fig. 2 in the main manuscript) are shown in Fig. S2 and S4. In Fig. S3, we compare, for BN-capped WS₂/Gr excited at 633 nm, the computed values of γ^{VH} , $\gamma^{+45^\circ, -45^\circ}$ and ρ^+ are compared to our normalized measurements of m_{11} , m_{22} , m_{33} , respectively. Since the off-diagonal elements of \mathcal{M} are vanishingly small, we indeed do not observe any significant differences between the polarization contrasts and m_{ii} , $i = 1..3$. In Fig. S5, we also show direct measurements of ρ^+ for another WS₂/Gr sample.

S3.1. Polarimetry measurements on WS₂/Gr

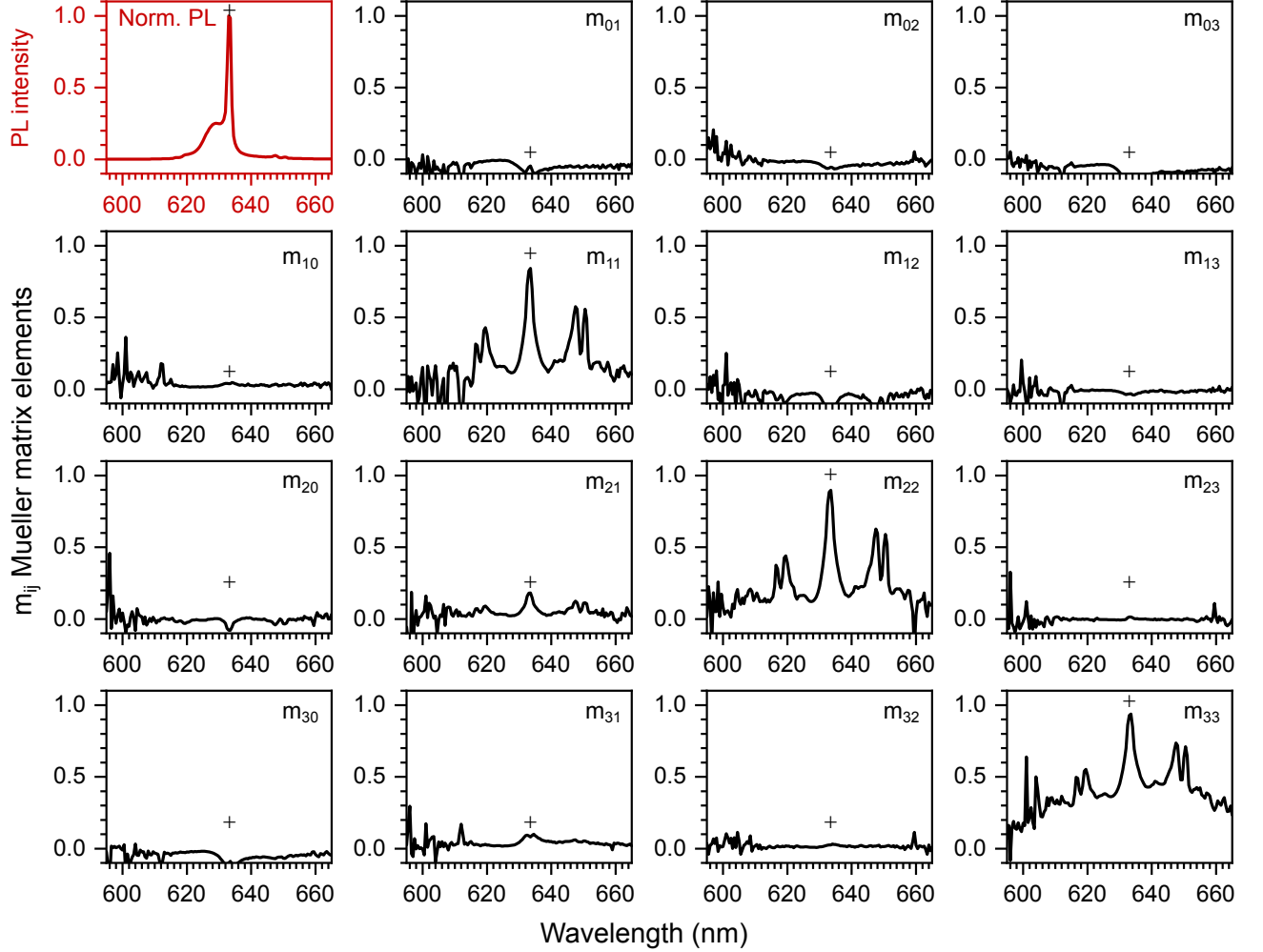


FIG. S2. Mueller matrix of the PL emission from our BN-capped WS₂/Gr heterostructure recorded in ambient conditions under optical excitation at 633 nm. The + symbols highlight residual contributions from the laser beam.

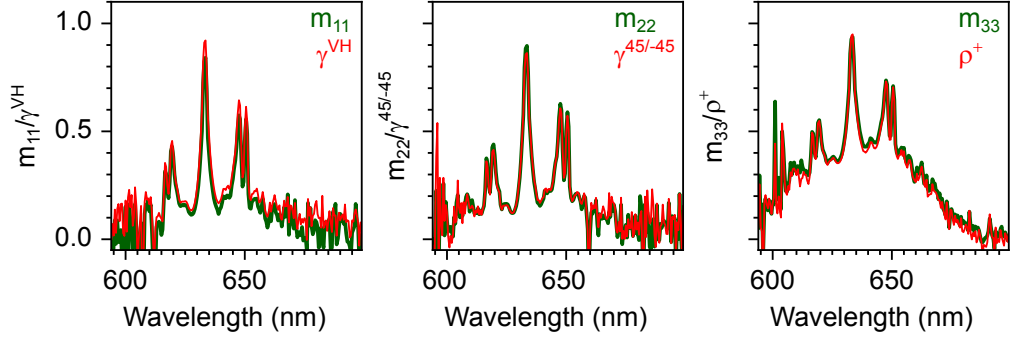


FIG. S3. BN-capped WS_2/Gr valley polarization and coherence recorded in ambient conditions under optical excitation at 633 nm: comparison between the diagonal terms of the Mueller matrix (green) and the PL linear and circular polarization contrasts (red) computed according to Eq. S8. The + and * symbols highlight residual contributions from the laser beam and polarization contrasts from WS_2 Raman scattering features, respectively.

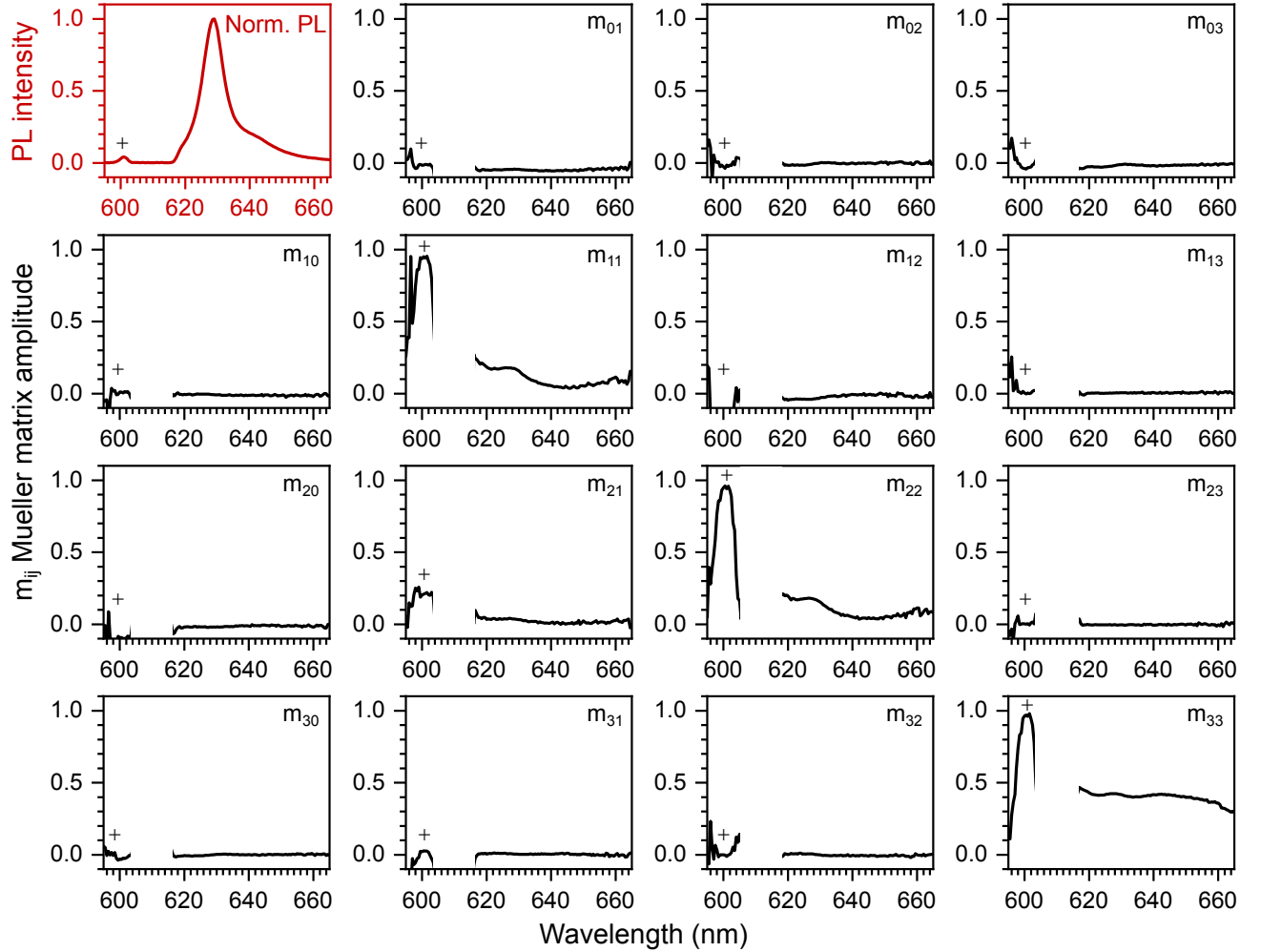


FIG. S4. Mueller matrix of the PL emission from our BN-capped WS_2/Gr heterostructure recorded in ambient conditions under optical excitation at 600 nm. The + symbols highlight residual contributions from the laser beam.

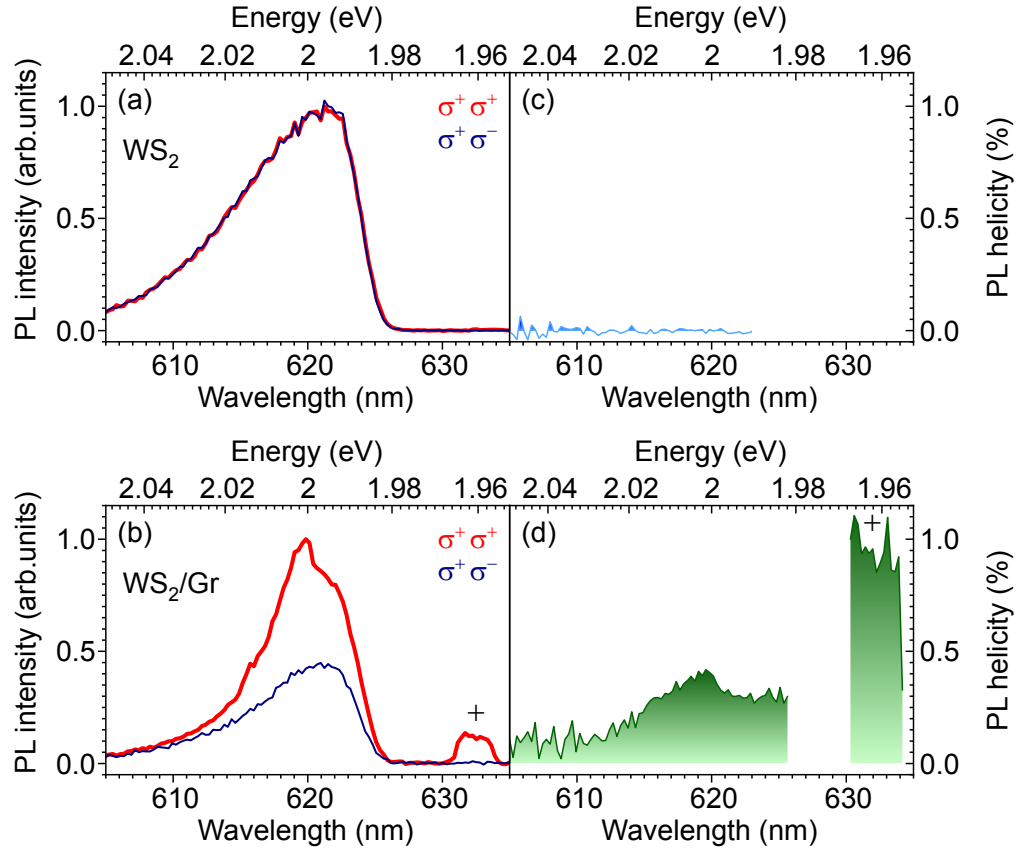


FIG. S5. Polarization-resolved PL spectra of (a) WS₂ and (b) WS₂/Gr recorded in ambient conditions for σ_{\pm} polarized light at 1.96 eV (i.e., 633 nm). The samples are excited using σ_+ polarized light. The corresponding degrees of circular polarization are shown in (c) and (d). Significant helicity (up to 25%) is only observed in WS₂/Gr. The sample is deposited on a SiO₂ substrate and capped with a LiF epilayer.

S3.2. Polarimetry measurements on MoSe₂/Gr

The Mueller matrix for BN-capped MoSe₂/Gr excited at 780 nm is reported in Fig. S6. The diagonal terms of the Mueller matrix of MoSe₂/Gr excited at 1.50 eV (i.e., 825 nm), slightly below the optical bandgap of MoSe₂ are shown in Fig. S7.

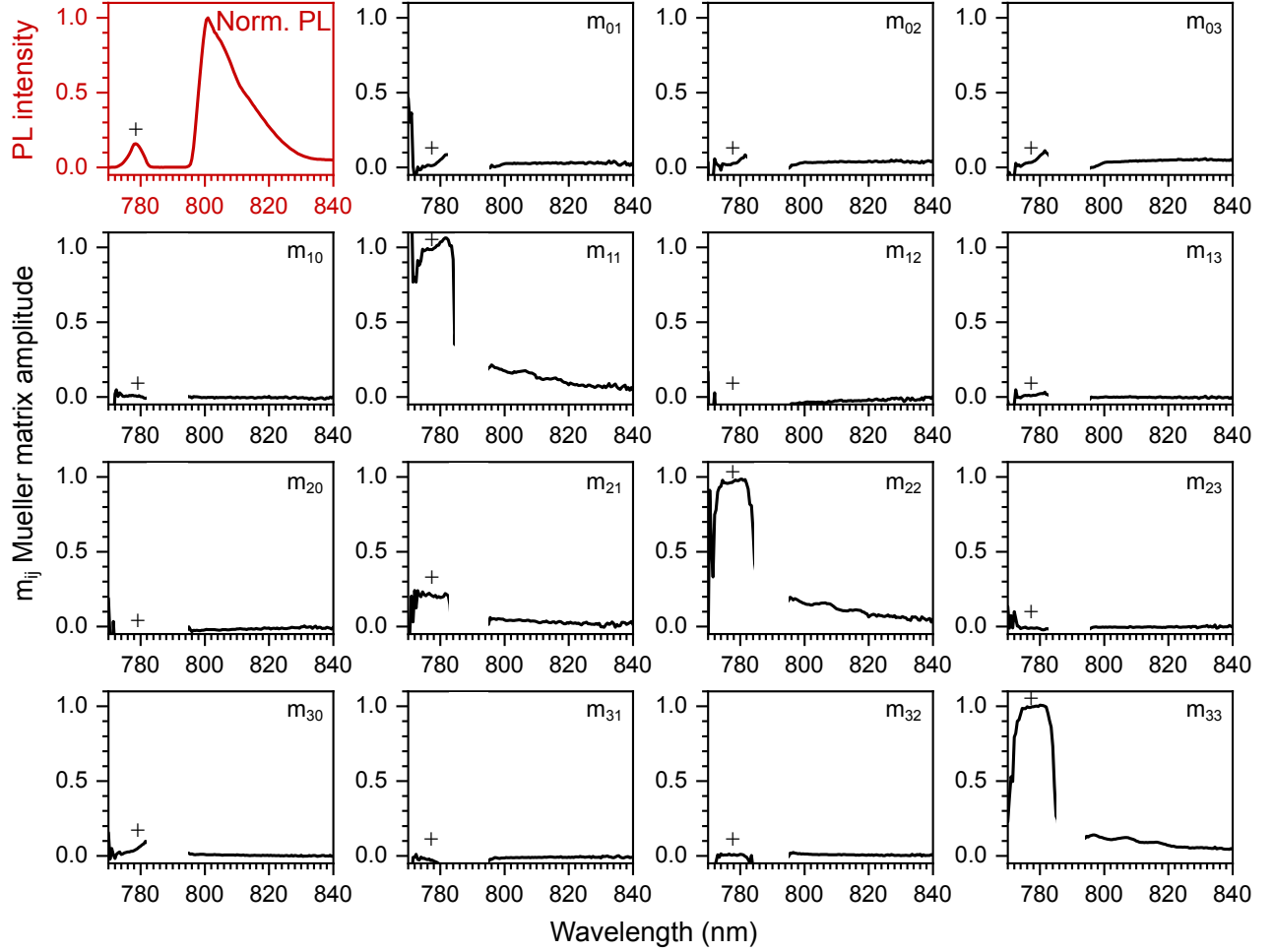


FIG. S6. Mueller matrix of the PL emission from our BN-capped MoSe₂/Gr heterostructure recorded in ambient conditions under optical excitation at 780 nm. The + symbols highlight residual contributions from the laser beam.

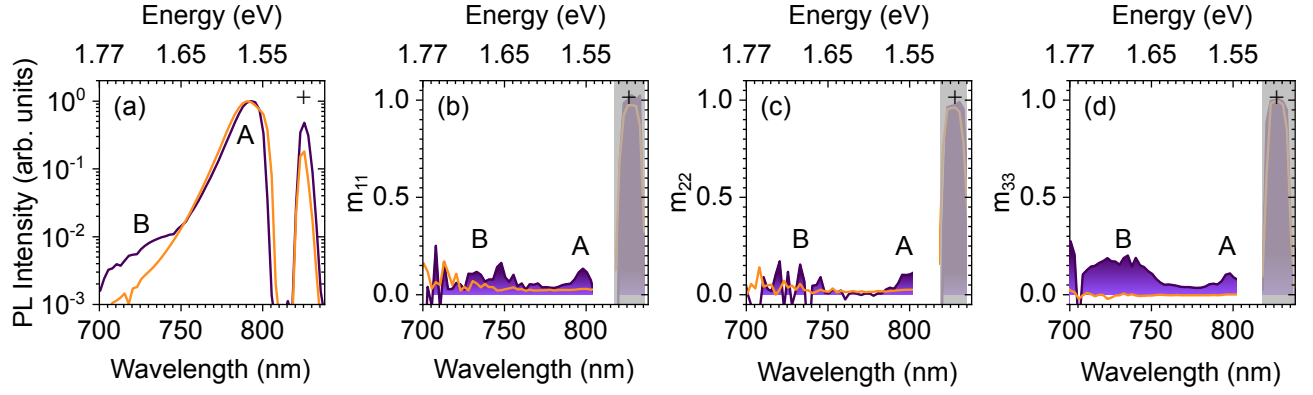


FIG. S7. BN-capped MoSe₂/Gr valley polarization and coherence: PL spectra (m_{00}) and spectrally resolved diagonal terms of the Mueller matrix (m_{ii} , $i = 1, 2, 3$) of a BN-capped MoSe₂/Gr sample under sub-bandgap optical excitation at 825 nm (i.e., 1.50 eV). The purple (resp. orange) curves correspond to BN-capped MoSe₂/Gr (resp. BN-capped MoSe₂). The + symbols highlight residual contributions from the laser beam. Under sub-bandgap excitation, exciton formation may occur through phonon assisted [53, 54] or possibly two-photon upconversion processes [54]. We observe nearly equal valley polarization and coherence, both of up to 12% at the A exciton peak energy, in BN-capped MoSe₂. Let us note that, unexpectedly, we are still able to resolve very dim upconverted PL from the B exciton in BN-capped MoSe₂/Gr, which displays degrees of valley polarization and coherence of up to 16% and $\sim 5 - 10\%$, respectively. No measurable emission from the B exciton is observed in BN-capped MoSe₂ under sub-bandgap excitation.

S3.3. High-resolution Raman scattering spectroscopy on WS_2/Gr

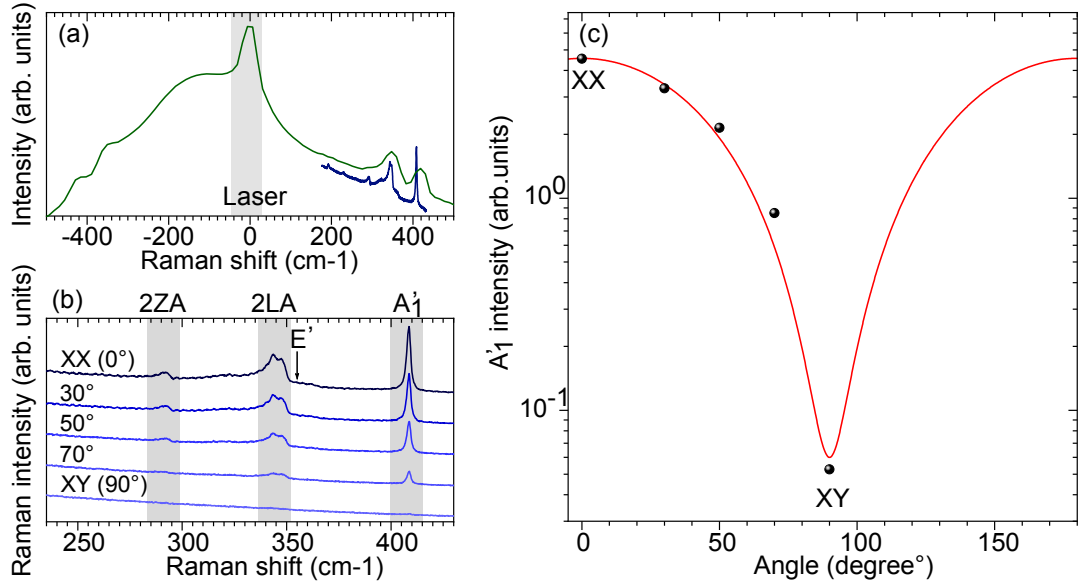


FIG. S8. (a) Green: PL spectrum of BN-capped WS_2/Gr (see Fig. 1 in the main text). Blue: high-resolution Raman spectrum, recorded in ambient conditions using a spectrometer with 500 mm focal length and a 2400 grooves/mm grating. Both spectra are recorded under linearly polarized optical excitation at 633 nm. The expected position the E' mode feature is indicated 41. (b) Polarization-resolved Raman spectra for parallel (XX) and perpendicular (XY) linear polarizations of the incoming and scattered photons. The main features are indicated, as in Ref. 41. (c) Integrated intensity of the out-of-plane A_1' feature as a function of the angle between the linearly polarized incoming and scattered photons. The solid line is a \cos^2 fit to the data.

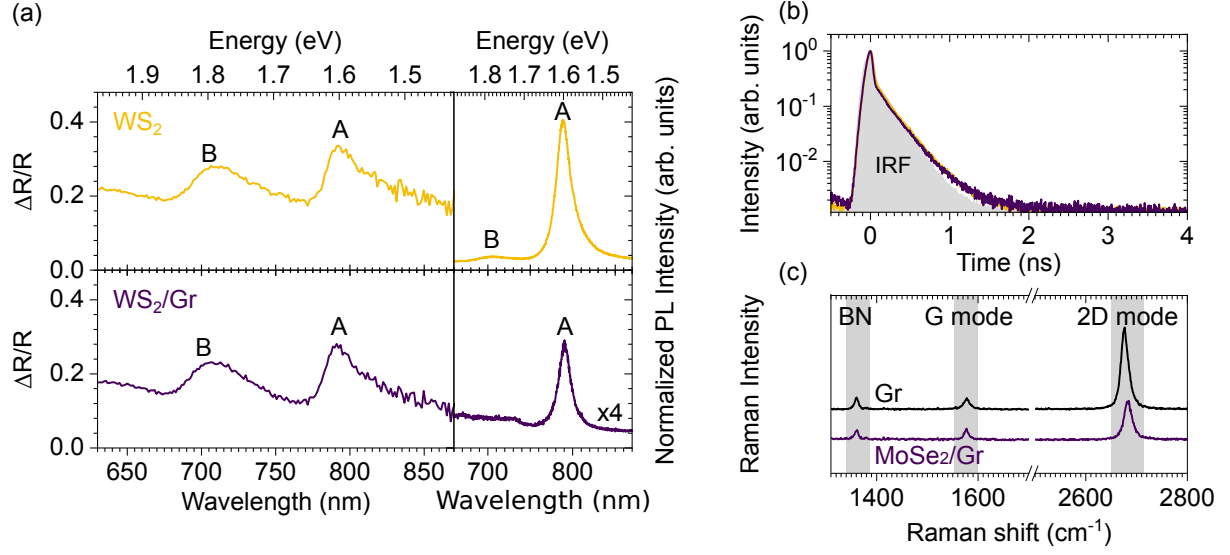
S3.4. Optical characterization of MoSe₂/Gr

FIG. S9. (a) Differential reflectance (DR) and PL spectra of BN-capped 1L-MoSe₂ (yellow) and BN-capped 1L-WS₂/Gr (purple). The PL spectra were recorded in the linear regime, under *cw* laser illumination at 532 nm (2.33 eV). (b) PL decay of BN-capped 1L-MoSe₂ (yellow) and BN-capped 1L-WS₂/Gr (purple) recorded under pulsed excitation at 480 nm (2.58 eV). The instrument response function (IRF) is represented by the grey area. The PL decays of BN-capped MoSe₂ cannot be resolved. Nevertheless Significant PL quenching by a factor of 6 is observed on BN-capped MoSe₂/Gr, indicating a shorter exciton lifetime as compared to BN-capped MoSe₂/Gr. (c) Raman spectra of BN-capped graphene and BN-capped MoSe₂/graphene under optical excitation at 532 nm.